

# Wall-modeled LES of the Boeing speed bump using a non-Boussinesq modeling framework

By R. Agrawal, S.T. Bose<sup>†</sup> AND P. Moin

## 1. Motivation and objectives

In the limit of increasingly large Reynolds numbers, the feasibility of direct numerical simulations (DNS) of the Navier-Stokes equations becomes impractical. A widely used tool aimed at alleviating this issue is the large-eddy simulation (LES) methodology, wherein the simulations are coarse-grained relative to a DNS. The large eddies in the flow are resolved numerically, but the unresolved eddies are modeled using physics-inspired phenomenological models (Smagorinsky 1963; Germano *et al.* 1991; Nicoud *et al.* 2011; Vreman *et al.* 1994).

A commonly utilized framework for subgrid-scale (SGS) modeling is the eddy-viscosity formulation using both static (Smagorinsky 1963; Vreman 2004; Rozema *et al.* 2015) and dynamic methods (Germano *et al.* 1991; Ghosal *et al.* 1995; Meneveau *et al.* 1996). The dynamic procedure (based on the idea of test filtering) was introduced to alleviate the ad hoc prescription of a model coefficient to the numerous SGS models depending on the flow. However, in all of these formulations, the SGS stresses are assumed to be locally aligned and scaled with the strain rates of the resolved eddies, thus acting as a further diffusive source of momentum in addition to the molecular viscosity. Recently, Agrawal *et al.* (2022) showed that in both *a-priori* and *a-posteriori* calculations, a non-Boussinesq formulation of the SGS stresses, or the dynamic tensor-coefficient Smagorinsky model (DTCSM), outperforms the classical eddy-viscosity models.

For wall-bounded turbulence, as the Reynolds number increases, the size of the largest energy-containing eddies in the outer part of the boundary layer becomes increasingly large compared to the near-wall eddies. This means that significant grid refinement close to the wall is required to accurately resolve the near-wall eddies, even within the LES paradigm. Choi & Moin (2012) suggest that the grid requirements for such calculations scale with a super-linear power of the Reynolds number, thus making the numerical simulations expensive. To reduce the issues related to this intractability, the effect of the subgrid, near-wall flow within the turbulent boundary layer is modeled, and this method is referred as wall-modeled LES (WMLES).

Traditionally, wall-modeling practices include wall-stress models which supply a flux (or wall stress) to the outer LES solution in the form of a boundary condition. These wall models are principally motivated by the Reynolds-averaged Navier-Stokes (RANS) form of the thin-boundary-layer equations (see Bose & Park (2018) for more details). One of the most commonly used wall models is the equilibrium wall model (EQWM), in which the near-wall eddies are assumed to be in local equilibrium. In this framework, a non-zero flux is supplied to the outer LES in the streamwise and spanwise directions, with the non-penetrating Dirichlet boundary condition. This model has been successfully applied in both canonical flows (Kawai & Larsson 2012; Lozano-Durán & Bae 2019) and

<sup>†</sup> Cascade Technologies

flows over complex geometries of engineering interest (Lozano-Durán *et al.* 2020; Goc *et al.* 2021).

It is noteworthy that for flows that suffer mild adverse pressure gradients, such as the Boeing speed bump flow, the combined modeling choices of the dynamic Smagorinsky subgrid-scale model (DSM) and the EQWM suffer from a non-monotonic collapse of the separation bubble on grid refinement (Whitmore *et al.* 2021). This was rectified by using the DTCSM to achieve monotonic convergence (Agrawal *et al.* 2022). However, the grid requirements ( $\delta/\Delta \sim 15\text{--}20$  where  $\Delta$  is the grid resolution and  $\delta$  is the boundary layer thickness) necessary for both the DSM and DTCSM to reasonably predict the coefficients of pressure and skin friction, can potentially restrict efficient adaption into industrial design methods due to the increased Reynolds numbers. For example, on a full-scale aircraft at flight Reynolds numbers, these grid requirements would total up to  $O(10^9)$  grid points. Furthermore, it is expected that the assumptions involved in developing the EQWM do not strictly hold in the presence of strong pressure gradients (in comparison to wall shear) as the large eddies are not under statistical equilibrium.

In this brief, we develop an approach that does not involve *a-priori* knowledge of the flow characteristics and improves the predictive capabilities of LES in flows undergoing smooth-body separation at coarser than  $\delta/\Delta \sim 15\text{--}20$ . For these purposes, a dynamic sensor for predicting turbulent separation bubbles in the presence of adverse pressure gradients has been developed and validated in smooth-body separation experiments such as the Boeing speed bump (Gray *et al.* 2021; Williams *et al.* 2020).

The rest of the brief is organized as follows. We provide the equations for LES formulation and revisit the non-Boussinesq SGS model, DTCSM, in Section 2. Section 3 details the conventional RANS-motivated equilibrium wall-modeling paradigm, followed by the development of a dynamic sensor to detect separation. Some details of the numerical solver used in this work are provided in Section 4. A detailed *a-posteriori* analysis of the performance of the existing and proposed models for the flow over a Gaussian bump exhibiting separation is presented in Section 5. Conclusions are provided in Section 6.

## 2. LES formalism and governing equations

In LES, the coarse-grained, Reynolds-averaged, large-scale quantities are defined by filtering the primitive fields. Denoting the grid-filter kernel operator by  $\mathcal{G}$ , the large-scale quantity,  $\tilde{f}$ , can be evaluated from the total field,  $f$ , as

$$\tilde{f}(x) = \int \mathcal{G}(x, x') f(x') dx', \quad (2.1)$$

where the integral is extended over the entire simulation domain. Similarly, we define  $\bar{f}$  to be a Favre-averaged variable as

$$\bar{f} = \frac{\tilde{f}\rho}{\bar{\rho}}. \quad (2.2)$$

More details on the LES formalism can be found in previous studies (Moin *et al.* 1991; Germano *et al.* 1991; Ghosal *et al.* 1995; Fu *et al.* 2021).

With these definitions, for a compressible turbulent flow (of internal energy  $e$ , density  $\rho$ , temperature  $T$ , viscosity  $\mu(T)$ , and thermal conductivity  $\kappa(T)$ ) and velocity vector  $\vec{u} = \{u_1, u_2, u_3\}$ , the governing equations can be obtained by applying the aforementioned filters to the Navier-Stokes equations to arrive at

$$\frac{\partial \tilde{\rho}}{\partial t} + \frac{\partial(\tilde{\rho} \bar{u}_i)}{\partial x_i} = 0, \quad (2.3)$$

$$\frac{\partial(\tilde{\rho} \bar{u}_i)}{\partial t} + \frac{\partial(\tilde{\rho} \bar{u}_j \bar{u}_i)}{\partial x_j} = -\frac{\partial \tilde{p}}{\partial x_i} + \frac{\partial(\mu \overline{S_{ij}^d})}{\partial x_j} - \frac{\partial \tau_{ij}^{sgs}}{\partial x_j}, \quad (2.4)$$

and

$$\frac{\partial \tilde{E}}{\partial t} + \frac{\partial(\tilde{E} \bar{u}_j)}{\partial x_j} = -\frac{\partial(\tilde{p} \bar{u}_i)}{\partial x_i} + \frac{\partial(\mu \overline{S_{ij}^d} \bar{u}_i)}{\partial x_j} - \frac{\partial(\tau_{ij}^{sgs} \bar{u}_i)}{\partial x_j} - \frac{\partial Q_j^{sgs}}{\partial x_j} + \frac{\partial}{\partial x_j} \left( \kappa \frac{\partial \tilde{T}}{\partial x_j} \right), \quad (2.5)$$

where  $\tilde{E} = \tilde{\rho}(\bar{e} + 0.5 \bar{u}_i \bar{u}_i)$  is the sum of the resolved internal and kinetic energies and  $\overline{S_{ij}^d}$  is the deviatoric part of the resolved strain-rate tensor.

Note that  $\tau_{ij}^{sgs} = \tilde{\rho}(\bar{u}_i \bar{u}_j - \bar{u}_j \bar{u}_i)$  and  $Q_j^{sgs} = \tilde{\rho}(\bar{e} \bar{u}_j - \bar{e} \bar{u}_j)$  are the subgrid stress and heat flux, respectively, which require modeling closure. The isotropic component of the subgrid stress is often absorbed into pressure, which leads to a pseudo-pressure field. The subgrid heat flux is modeled using the constant turbulent Prandtl number approximation ( $Pr_t = 0.9$ ) based on the dissipative component of the subgrid-stress tensor. The next subsection describes the non-Boussinesq model recently developed by Agrawal *et al.* (2022).

### 2.1. Dynamic tensor-coefficient Smagorinsky model

Germano *et al.* (1991) introduced the concept of test filtering of the LES governing equations that allowed one to relate the resolved turbulent stresses,  $L_{ij} = -\widehat{\tilde{\rho} \bar{u}_i \bar{u}_j} + \widehat{\tilde{\rho}} \widehat{\bar{u}_i} \widehat{\bar{u}_j}$ , where  $\widehat{(\cdot)}$  denotes test-filter operation to the modeled stresses.

For LES of flows with mean flow-driven anisotropy (for example, turbulent boundary layers), the assumption of a scalar model coefficient that is agnostic to the anisotropy direction is potentially inappropriate. Agrawal *et al.* (2022) developed a novel non-Boussinesq SGS model which uses dynamic tensorial coefficients. Mathematically, this tensor-coefficient model can be written as

$$\tau_{ij}^{sgs} - \frac{\tau_{kk}^{sgs}}{3} \delta_{ij} = -(C_{ik} \overline{S_{kj}^d} + C_{jk} \overline{S_{ki}^d}) |S| \tilde{\rho} \Delta^2, \quad (2.6)$$

where  $|S| = \sqrt{2 \overline{S_{ij}^d} \overline{S_{ij}^d}}$ . In its general form, this model contains nine independent coefficients; however, Agrawal *et al.* (2022) argued that for this model to satisfy its tracelessness property, the coefficients can be related to one another as

$$C_{11} = C_{22} = C_{33}; \quad C_{ij} = -C_{ji} \quad (j \neq i). \quad (2.7)$$

These realizability constraints reduce the number of independent coefficients from nine to four. Applying the Germano identity to this model form, the following system of equations is derived and then eventually solved in the least-squares sense to dynamically compute all model coefficients as

$$L_{ij} = (C_{ik} \Delta^2 M_{kj} + C_{jk} \Delta^2 M_{ki}), \quad (2.8)$$

where

$$M_{ij} = \left( \frac{\widehat{\Delta}^2}{\Delta^2} \widehat{\tilde{\rho}} |S| \overline{S_{ij}^d} - \tilde{\rho} |S| \overline{S_{ij}^d} \right) \quad (2.9)$$

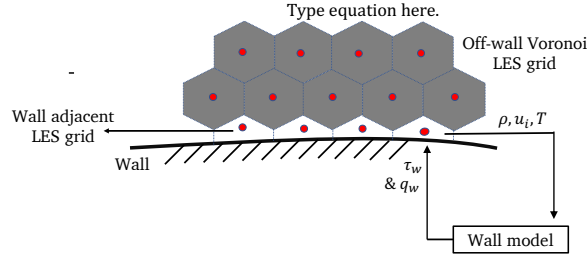


FIGURE 1. Schematic of a WMLES grid with the wall stress predicted by the wall model applied in the wall-adjacent cell. Note that the red dots represent the cell centers where the primitive variables are stored. The wall model takes the cell density, velocity and temperature as inputs, and provides a shear stress, and heat flux that act on the wall-neighboring cell.

and where  $\hat{\Delta}$  and  $\Delta$  denote test-level and grid-level filter widths, respectively. Further details about the model formulation, the implementation of the dynamic procedure, and the averaging operation for avoiding numerical instabilities are given in Agrawal *et al.* (2021, 2022).

### 3. Wall-model specification

This section provides a brief discussion of the traditional equilibrium wall modeling procedure. Next, a novel framework is presented which includes the development of the dynamic separation prediction sensor, along with the corrections made to the EQWM in presence of mean flow non-equilibrium.

#### 3.1. Equilibrium wall model

Consider an LES grid designed to minimally resolve the large scales in the outer layer of the boundary layer ( $\delta/\Delta \sim O(10-20)$ ), such as in Figure 1.

The equilibrium wall model assumes that a constant stress layer across the unresolved inner layer exists, and this stress can be provided to the outer solution using a Neumann boundary condition. Under the assumptions of equilibrium, no external mean pressure gradients, and slow variations in the mean velocity (denoted as  $U_{||}$ ) in the streamwise and spanwise directions, the mean wall-parallel momentum equations can be locally written as

$$\frac{d}{dy} [(\mu + \mu_{wm}) \frac{dU_{||}}{dy}] = 0. \quad (3.1)$$

Equation 3.1 can be integrated along the wall-normal direction between  $y = 0$  (wall) and  $y = h_{wm}$  (outer LES matching location) to derive an inner-layer mean velocity profile which can be used to calculate the wall shear stress as a boundary condition for the outer flow. Cabot & Moin (2000) proposed a form of  $\mu_{wm}$  to recover the equilibrium law of the wall for flow over a smooth flat plate under zero pressure gradient conditions, given as

$$\mu_{wm} = \kappa \rho y \sqrt{\frac{\tau_w}{\rho}} (1 - \exp(-y^+/A^+))^2, \quad (3.2)$$

where  $\kappa = 0.38$  is the von-Kármán constant,  $A^+ = 17$  is a calibrated constant to recover the law of the wall in a zero pressure gradient boundary layer, and  $\tau_w$  is the wall shear

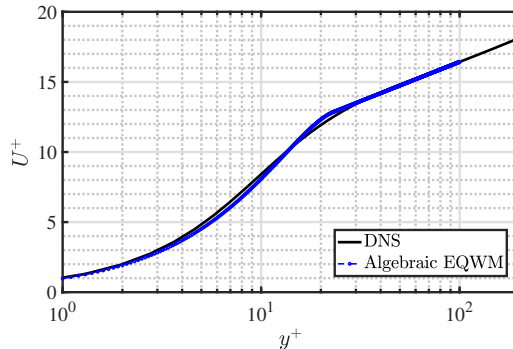


FIGURE 2. A comparison between the DNS mean velocity profile of a turbulent channel flow at  $Re_\tau = 4200$  and the algebraic EQWM used in the charLES flow solver.

stress. The superscript  $(\cdot)^+$  denotes inner-unit variables (length and velocity scaling based on the wall stress and viscosity).

For flows without significant compressibility effects, it is often sufficient to specify an approximate analytical solution to the above differential equation. One such solution is used in this brief; in inner units, the mean streamwise velocity profile is determined as

$$u^+(y^+) = \begin{cases} y^+ + a_1(y^+)^2 & \text{if } y^+ \leq 23, \\ \frac{1}{\kappa} \ln(y^+) + B & \text{otherwise,} \end{cases} \quad (3.3)$$

where  $B = 5.2$ ,  $\kappa = 0.41$ , and  $a_1$  is chosen to ensure  $\mathcal{C}^1$  continuity in the piecewise velocity profile. For reference, Figure 2 compares the mean wall-parallel velocity as a function of wall-normal coordinates in inner units ( $y^+$ ) for a high Reynolds number turbulent channel flow ( $Re_\tau = 4200$  channel in Lozano-Durán & Jiménez (2014)). As expected, the wall-modeled velocity profile agrees very well with the DNS mean velocity profile for both small and large wall-normal distances. Finally, first-point matching has been used for all the results discussed in this brief.

### 3.2. Dynamic predictive sensor for flow separation

In a flow under non-equilibrium, the assumptions built into the EQWM are violated, for example, in the vicinity of a turbulent separation bubble as there is a non-zero three-dimensional pressure gradient affecting the flow. Since the assumption of a universal law of the wall is valid only for flows under equilibrium, the application of the EQWM to complex separated flows is not fully justified. However, at sufficiently refined grids, such as when the grid resolutions are approximately  $y^+ \sim 5\text{--}20$ , the eddies are sufficiently resolved, which leads to the accurate prediction of the shear stress. Given these challenges, this work attempts to improve the predictions of the EQWM by leveraging the knowledge of the pressure gradients and the subgrid stresses in the vicinity of and inside the separation bubble.

Consider a wall-bounded flow being driven by a mean shear and mean pressure gradient (a favorable pressure gradient accelerates the flow, and an adverse pressure gradient decelerates it). The two characteristic velocity scales for this flow are the skin-friction velocity,  $\vec{u}_\tau$ , and the pressure-gradient based velocity,  $\vec{u}_p$ . Simpson (1983) provided a mean velocity scaling for the backflow in a turbulent separation bubble, a region which is dominated by adverse pressure gradient effects.

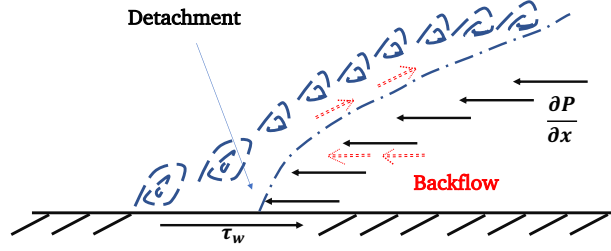


FIGURE 3. Schematic of case IV, a turbulent boundary layer subjected to an adverse pressure gradient (before separation) such that  $|u_p| > |u_\tau|$ .

For completeness, the mathematical forms of the two velocity scales are given as

$$\vec{u}_{\tau,i} \sim \left(\frac{\mu}{\rho} \frac{\partial U_i}{\partial n}\right)^{1/2} \quad \text{and} \quad \vec{u}_{p,i} \sim \left(\frac{\mu}{\rho^2} \frac{\partial P}{\partial x_i}\right)^{1/3}, \quad (3.4)$$

where  $n$  denotes the wall-normal direction, and  $i \in \{1, 2, 3\}$ . These two effects (or equivalently the velocity scales) can act along complementary directions or compete against each other, which can lead to four different conditions,

- (a) case I:  $\vec{u}_p \cdot \vec{u}_\tau > 0$ ;  $|\vec{u}_p| < |\vec{u}_\tau|$ ,
- (b) case II:  $\vec{u}_p \cdot \vec{u}_\tau > 0$ ;  $|\vec{u}_p| > |\vec{u}_\tau|$ ,
- (c) case III:  $\vec{u}_p \cdot \vec{u}_\tau < 0$ ;  $|\vec{u}_p| < |\vec{u}_\tau|$ ,
- (d) case IV:  $\vec{u}_p \cdot \vec{u}_\tau < 0$ ;  $|\vec{u}_p| > |\vec{u}_\tau|$ .

For cases I and II, the pressure gradient is favorable with respect to skin friction, and vice versa for cases III and IV. In cases I and III, skin friction dominates the pressure gradient effects, and the equilibrium conditions are only weakly violated. However, in cases II and IV, the pressure gradient effects dominate the equilibrium velocity prediction due to skin friction. It is then justifiable that the equilibrium model alone cannot be relied upon in cases II and IV, since the dominant terms (pressure gradients) are ignored (or considered small) in the derivation of the equilibrium wall model. The reader is directed to Appendix A for demonstration of the proof of concept of this sensor for two canonical cases of wall-bounded flows, namely the turbulent channel flow and a zero pressure gradient flat-plate boundary layer.

### 3.3. Non-equilibrium corrections to the equilibrium wall model

Balakumar *et al.* (2014) and Lozano-Durán *et al.* (2020) have previously reported the adequacy of the EQWM in mild favorable pressure gradient regimes in flow over a periodic hill and in spanwise-excited, non-equilibrium turbulent channel flow. This is presumably related to the observation that the mean streamwise velocity still obeys a log-law (with a modified intercept,  $B$ ) in favorable pressure gradient regimes.

For flows that experience adverse pressure gradient driven separation, Adams & Johnston (1988) experimentally showed that although the mean velocity profile inside a separation bubble resembles a laminar, Falkner-Skan shape, the root mean square of the fluctuations of the velocities is high, and so the flow is turbulent. Furthermore, in coarse WMLES, near the separation point, the shear stress is small. Under these conditions, the EQWM may predict excessively low wall stress (as most of the turbulent fluctuations within the separation bubble are subgrid, and moreover, in this regime which is dominated by adverse pressure gradients, the equilibrium assumptions are violated). Thus, for such coarse grids, the role of the SGS model becomes increasingly important within

the separation bubble. The eddy viscosity for the EQWM in Eq. (3.1) is tuned for a flow under equilibrium. Thus, for non-equilibrium flow, an additional component of the subgrid shear stress needs to be modeled.

In this brief, this non-equilibrated, fluctuating stress on the wall is modeled through an instantaneous Neumann extrapolation of the subgrid stresses in the wall-adjacent cell ( $\partial\tau_{ij}^{sgs}/\partial\hat{n}_j = 0$ , where  $\hat{n}_j$  is the  $j$ th component of the wall-normal unit vector directed into the fluid). It is assumed that the subgrid stress in the wall-adjacent cell is a suitable model for the non-equilibrium component of the wall stress.

Thus, the wall model can be summarized as

$$\tau_{w,i} = \begin{cases} \tau_{w,i}^{EQWM} & \text{if } |\overline{u_p}| < |\overline{u_\tau}|, \\ \tau_{w,i}^{EQWM} - \tau_{ij}^{sgs} \cdot n_j & \text{otherwise,} \end{cases} \quad (3.5)$$

where  $i, j \in \{1, 2, 3\}$  and  $\tau_{w,i}^{EQWM}$  denotes the wall stress predicted from the EQWM in the  $i$ th direction. The operator  $\overline{(\cdot)}$  denotes averaging (with an exponential memory) along the homogeneous direction. In the flows considered in this brief, there is no statistically homogeneous spatial direction, but the flows are statistically steady in time.

#### 4. Numerical solver details

All the simulations as presented in this brief were performed using an explicit, unstructured, finite-volume solver for the compressible Navier-Stokes equations (charLES). This code is formally second-order accurate in space and third-order accurate in time. More details of the solver and validation cases can be found in Brès *et al.* (2018) and Goc *et al.* (2021).

#### 5. Wall-modeled LES of flow over Gaussian bump

The geometry of the speed bump was developed jointly by Boeing and the Williams group at the University of Washington (Williams *et al.* 2020); the bump surface is defined by an analytical expression,  $h(x, z)$ , written as

$$h(x, z) = \frac{h_0}{2} e^{-(x/x_0)^2} \left\{ 1 + \operatorname{erf} \left[ \left( \frac{L}{2} - 2z_0 - |z| \right) / z_0 \right] \right\}, \quad (5.1)$$

where  $x$  and  $z$  are the streamwise and spanwise coordinates, respectively. Note that  $h_0 = 0.085L$  is the maximum height of the bump, and  $x_0 = 0.195L$  controls the Gaussian decay of the surface along the  $x$  direction. Similarly,  $z_0 = 0.06L$  controls the decay in the spanwise direction,  $z$ . The Reynolds number,  $Re_L$ , for this flow is defined in terms of the upstream freestream velocity  $U_\infty$  and bump width  $L$ . Fig. 4 represents the schematics of the true experimental geometry.

The flow over the bump experiences a strong favorable pressure gradient followed by a strong adverse pressure gradient on the fore and aft sections of the bump, respectively. This leads to the formation of a turbulent separation bubble at the presently considered Reynolds numbers,  $Re_L = 2 \times 10^6$  and  $Re_L = 3.4 \times 10^6$ . Previous experimental efforts (Williams *et al.* 2020; Gray *et al.* 2022) suggest an approximate Reynolds number independence of the separation bubble for  $Re_L > 2 \times 10^6$ . The geometry studied in the experimental setup has a tapered span, and wind tunnel side walls present some confinement and three-dimensional effects. Thus, this flow stands as a canonical candidate for

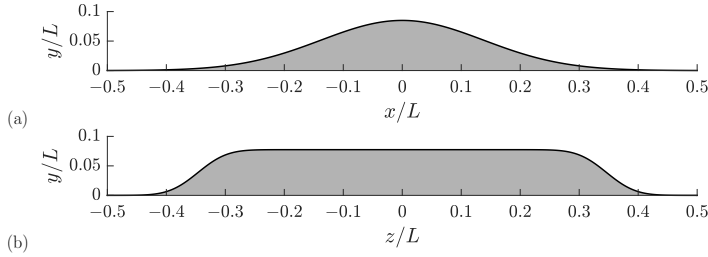


FIGURE 4. Cross sections of the three-dimensional bump geometry. The geometry has side walls at  $z/L = \pm 0.5$  and a top wall at  $y/L = 0.5$ . Note that the spanwise-periodic bump has the same cross-sectional profile as the three-dimensional bump; however, the spanwise direction is periodic with  $z/L$  spanning from 0–0.08, and the top wall is at  $y/L = 1.0$ . Figure and caption reproduced with permission from Agrawal *et al.* (2022).

assessing the performance of existing and future LES models for smooth-body separation experiments.

It is expected that the resolution required for performing a DNS of the three-dimensional experimental geometry would involve  $O(10^{11})$  points and hence would be intractable for practical purposes. Uzun & Malik (2022) performed a quasi-DNS (the grid resolution of the separated shear layer resembles an LES, with no explicit SGS model being employed) of the spanwise-periodic variant geometry (which is representative of the midspan of the experimental configuration) with  $O(10^{10})$  mesh points. Furthermore, no side tapering in the spanwise direction was present in the quasi-DNS, with a bump height of  $h(x) = h_0 \exp(-x^2/x_0^2)$  and a spanwise extent of  $z/L = 0.08$ .

The quantities of interest for this flow are the skin-friction coefficient ( $C_f$ ) and the pressure coefficient ( $C_p$ ), which are defined as

$$C_f = \frac{\tau_w}{1/2\rho_\infty U_\infty^2} \quad \text{and} \quad C_p = \frac{p - p_{\text{ref}}}{1/2\rho_\infty U_\infty^2}, \quad (5.2)$$

where  $U_\infty$ ,  $\tau_w$ ,  $p$ , and  $p_{\text{ref}}$  are the inlet freestream velocity, mean wall stress, wall pressure, and reference pressure, respectively. Similar to Williams *et al.* (2020),  $p_{\text{ref}}$  is the wall pressure measured at  $x/L = -0.83$ .

The details of the case setup (domain extents, inlet conditions), boundary conditions, and the choice of computational meshes for both the spanwise-periodic and experimental configurations are identical to those of Agrawal *et al.* (2022) and are skipped here for brevity.

### 5.1. Spanwise-periodic configuration at $Re_L = 2 \times 10^6$

In this section, we compare WMLES results of the simulations of the spanwise-periodic Boeing speed bump configuration at  $Re_L = 2 \times 10^6$ . In Figures 5 and 6 (same as Figs. 13 and 14 in Agrawal *et al.* (2022)) the skin-friction and pressure coefficients are compared across different SGS models with the equilibrium wall model. It is quite apparent that the combination of DSM and EQWM leads to a non-monotonic convergence of  $C_f$  and  $C_p$  on grid refinement, whereas with the DTCSM, a monotonic convergence is observed. A more detailed discussion on the reporting of these results can be found in Agrawal *et al.* (2022).

Similar to Agrawal *et al.* (2022), in the current simulations presented in Fig. 7, the skin friction at the inlet is lower than the quasi-DNS; possibly due to the difference in the inlet boundary conditions (more details are available in Whitmore *et al.* (2021)). It

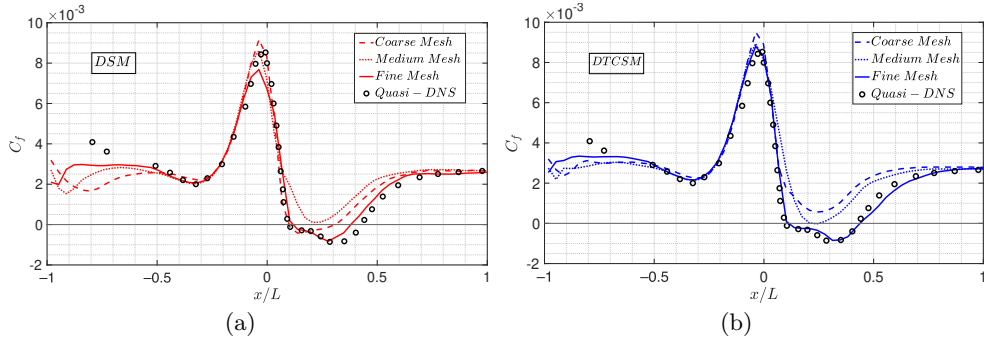


FIGURE 5. Streamwise distribution of the surface skin-friction coefficient for the spanwise-periodic bump at  $Re_L = 2 \times 10^6$  for (a) DSM and (b) DTCSM. The equilibrium wall model is applied, and three mesh resolutions are shown. The symbols represent the quasi-DNS of Uzun & Malik (2022). Figure reprinted with permission from Agrawal et al., Physical Review Fluids, Vol. 7, Iss. 7, pp. 074602, 2022. Copyright 2022 by the American Physical Society.

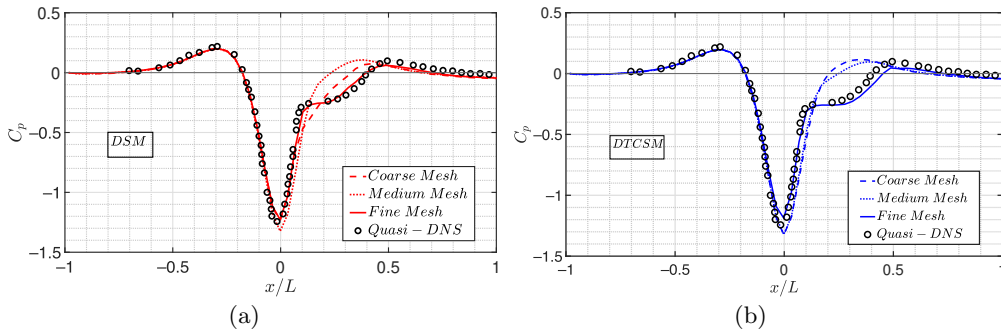


FIGURE 6. Streamwise distribution of the surface pressure coefficient for the spanwise-periodic bump at  $Re_L = 2 \times 10^6$  for (a) DSM and (b) DTCSM. The equilibrium wall model is applied, and three mesh resolutions are shown. The symbols represent the quasi-DNS of Uzun & Malik (2022). Figure reprinted with permission from Agrawal et al. Physical Review Fluids, Vol. 7, Iss. 7, pp. 074602, 2022. Copyright 2022 by the American Physical Society.

is expected, that due to the long development length of the inflow, the skin friction of the wall-modeled simulations does not represent that of fully developed, turbulent zero pressure gradient boundary layers. However, by  $x/L = -0.6$ , the simulations appear to have passed through the initial development length and nearly coincide with the quasi-DNS data in the favorable pressure gradient region.

The sensor-aided wall model is aimed to detect regions in a flow where the EQWM is expected to fail or incorrectly predict the wall shear stress. Based on the results in Figure 5, it is possible that the EQWM incorrectly predicts the shear stress in adverse pressure gradient regions when matched with outer LES at specific inner coordinates.

Figure 7 presents skin-friction and pressure-drag coefficients across the three meshes for the DTCSM and the sensor-aided EQWM. It is salient that the separation bubble is predicted on all grids considered, which is in line with previous observations on using the constant-coefficient slip wall model (Whitmore *et al.* 2021). The current results improve upon those observations in that the coarse grids do not have erroneous skin friction upstream of the bubble. On comparing these results with those in Figs. 5 and 6, it is

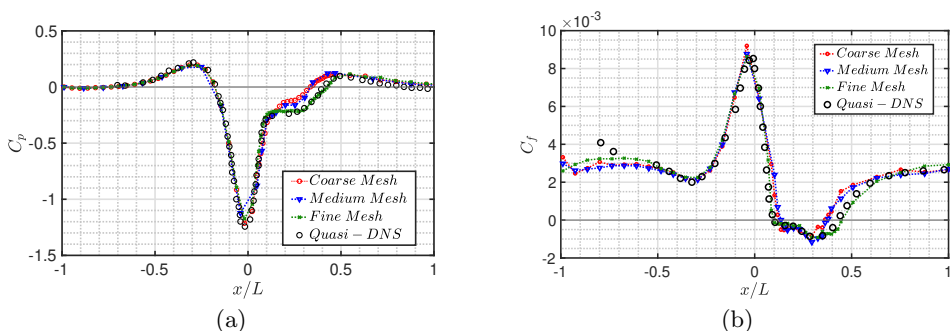


FIGURE 7. Streamwise distribution for the spanwise-periodic bump at  $Re_L = 2 \times 10^6$  of (a) the surface pressure coefficient and (b) the surface friction coefficient. The sensor-aided EQWM is applied, and three mesh resolutions are shown. The symbols represent the quasi-DNS of Uzun & Malik (2022).

apparent that most of the improvements appear on coarse and medium grids, which now predict a reasonably accurate extent and strength of the separation bubble. This is encouraging in that the separation characteristics are nearly accurate on relatively coarse grids. As also reported by Agrawal *et al.* (2022), the skin-friction peak is consistently captured on grid refinement by the combination of the DTCSM and sensor-aided EQWM.

From the plots of the skin friction and pressure drag, the action of the sensor appears to be limited primarily within the vicinity of the separation bubble. To verify that this is the case, the activity of the sensor is quantified. We define an activity parameter,  $\chi$  as

$$\chi(x) = \frac{1}{T} \int_0^T \frac{\gamma(x) + 1}{2} dt, \quad (5.3)$$

where

$$\gamma(x) = \text{sgn}(|\widetilde{u_\tau}(x)| - |\widetilde{u_p}(x)|), \quad (5.4)$$

and  $\widetilde{(\cdot)}$  is the running-average operator (up to a final time,  $T$ ) within a simulation, and  $\text{sgn}$  is the sign function. Note that within a simulation,  $\chi$  represents the running average of the extent to which the separation sensor remained active as a function of the streamwise distance. It is expected that in the regions where the equilibrium assumption strongly fails ( $|\widetilde{u_p}(x)| > |\widetilde{u_\tau}(x)|$ ), the activity parameter  $\chi$  will remain less than 1. Furthermore, for regions statistically resembling a zero pressure gradient boundary layer,  $\gamma(x) = 1$ .

Fig. 8(a) reflects the parameter  $\chi$  as a function of the streamwise distance (averaged in the periodic spanwise direction) for the fine-mesh result (although not shown, the other grids show similar qualitative behavior of the activity parameter). This plot conclusively shows that the sensor aids the EQWM in the upstream vicinity of, within, and in the downstream recovery region around the separation bubble. From the pressure gradient predictions in Fig. 7, this region coincides with the region of the adverse pressure gradient. Thus, the results seem consistent with the argument that the assumptions made in the EQWM primarily fail in the adverse pressure gradient regimes in this flow.

### 5.2. Three-dimensional configuration at $Re_L = 3.4 \times 10^6$

This section presents the WMLES results are presented for the experimental configuration given in Eq. (5.1) at a slightly higher Reynolds number of  $Re_L = 3.4 \times 10^6$  (the reference data were made available from the two separate experimental campaigns pur-

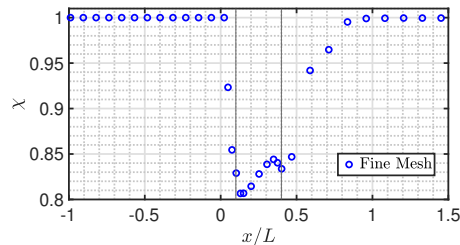


FIGURE 8. Streamwise distribution for the spanwise-periodic bump at  $Re_L = 2 \times 10^6$  of the spanwise-averaged activity parameter  $\chi$ . In the regions where  $\chi < 1$ , the sensor aids the EQWM in its prediction of the wall shear stress. Note that only one out of every three sampled points is plotted in the regions outside of  $0.1 < x/L < 0.5$  for visual clarity purposes. Furthermore, the two vertical lines at  $x/L = 0.1$  and  $0.4$  represent the approximate extent of the separation bubble, and  $0.4 < x/L < 0.7$  is the reattachment and recovery region of the separation bubble.

sued at the University of Washington and the University of Notre Dame). Williams *et al.* (2020) and Gray *et al.* (2022), have performed experimental measurements of the surface pressure, and skin friction respectively for the three-dimensional geometry. The slight tapering effect of the bump in the spanwise direction leads to a pressure-relieving effect (from inviscid theory) in the span, and also forms two counter-rotating vortices on the aft side of the bump.

The simulations considered in this brief will be compared to the prior work of Agrawal *et al.* (2022). Whitmore *et al.* (2021) also performed WMLES of this flow using the DSM and the constant-coefficient slip wall model, and predicted an accurate separation bubble (which was robust to grid refinement) on grid topology similar to that of the current work. However, similar to their results for the spanwise-periodic configuration, the predictions of the skin-friction coefficient upstream of the bump were not accurate. Iyer & Malik (2021) reported no separation in their WMLES calculations with the constant-coefficient Vreman model with up to 450 million CVs.

Agrawal *et al.* (2022) performed WMLES using the DTCSM and EQWM methodology, and observed a monotonically converging prediction of the skin-friction and pressure coefficients on the wall at midspan. However, fine grids (with the average height of the wall-neighboring cell,  $y_1^+$ , approximately equal to 30) were required to first observe the separation bubble ( $O(500)$  million CVs). Simulations involving the DSM and EQWM also showed a non-monotonic convergence, also similar to the spanwise-periodic case. Figs. 9 and 10 are reproduced to orient the reader to these observations.

The predictions of  $C_f$  and  $C_p$  with the proposed wall model are presented in Fig. 11. Similar to the observations for the spanwise-periodic geometry, a reasonably accurate separation bubble is predicted for the coarse and medium grids. On further refinement to the fine grid, the separation predictions improve further to match the experimental results. Across this grid refinement sweep, an approximate monotonic convergence toward the experiment is observed in both  $C_p$  and  $C_f$ . Both the suction peaks and the skin-friction peaks at the apex of the bump ( $x/L = 0$ ) are captured well.

On comparing across Figures 9–11, it is quite clear that the predictions of  $C_p$  and  $C_f$  on the coarse and medium grids improve significantly with the inclusion of the non-equilibrium corrections to the EQWM. Interestingly, in the recovery region ( $0.4 < x/L < 0.7$ ) of the separation bubble, the predictions with the sensor-aided wall model are consistently better than the DTCSM and EQWM simulations (see Fig. 9) across all grids.

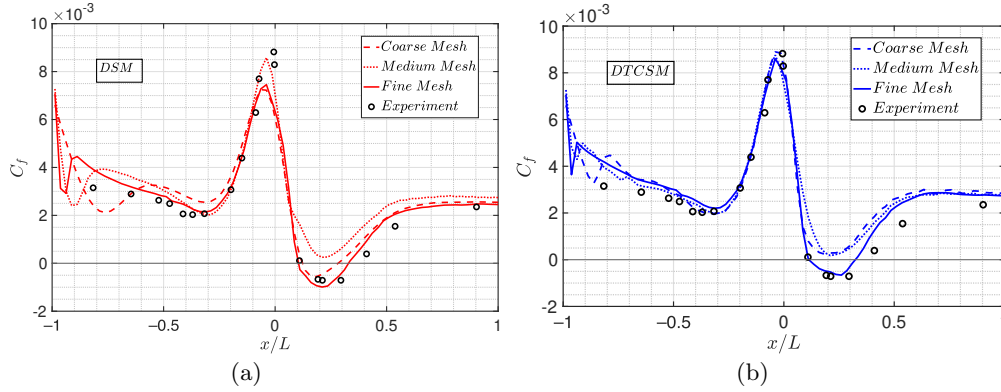


FIGURE 9. Streamwise distribution of the midspan surface friction coefficient for the three-dimensional bump at  $Re_L = 3.4 \times 10^6$  for (a) DSM and (b) DTCSM. The EQWM is applied, and three mesh resolutions are shown. The black dots represent the experiments performed by Gray *et al.* (2022). Figure reprinted with permission from Agrawal *et al.*, *Physical Review Fluids*, Vol. 7, Iss. 7, pp. 074602, 2022. Copyright 2022 by the American Physical Society.

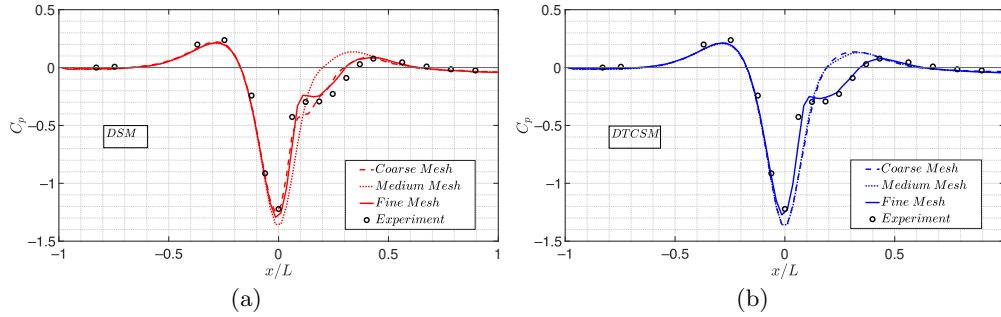


FIGURE 10. Streamwise distribution of the midspan surface pressure coefficient for the three-dimensional bump at  $Re_L = 3.4 \times 10^6$  for (a) DSM and (b) DTCSM. The black dots represent the experimental measurements of Williams *et al.* (2020). Figure reprinted with permission from Agrawal *et al.*, *Physical Review Fluids*, Vol. 7, Iss. 7, pp. 074602, 2022. Copyright 2022 by the American Physical Society.

The values of the activity parameter,  $\chi$ , for the spanwise-periodic configuration suggest that the sensor remains active in the recovery region. This highlights the importance of the choice of the SGS model in predicting the non-equilibrium processes in the recovery region.

From the observations on both the spanwise-periodic and experimental configurations, it is reasonably justifiable to argue that the addition of the sensor to the EQWM improves the results, especially in the vicinity of the separation bubble. It is likely possible that improved wall models such as the integral wall model of Yang *et al.* (2015) or the dynamic slip wall model (Bose & Moin 2014; Bae *et al.* 2019), can further improve the predictions of separation bubble over complex flows. Since the development and the implementation of the proposed sensor are agnostic to the choice of the SGS and wall model, the sensor shows promise in aiding the detection in the vicinity of a separation bubble. Finally, we note that Goc *et al.* (2022) report some improvements in the prediction of the lift, and moment

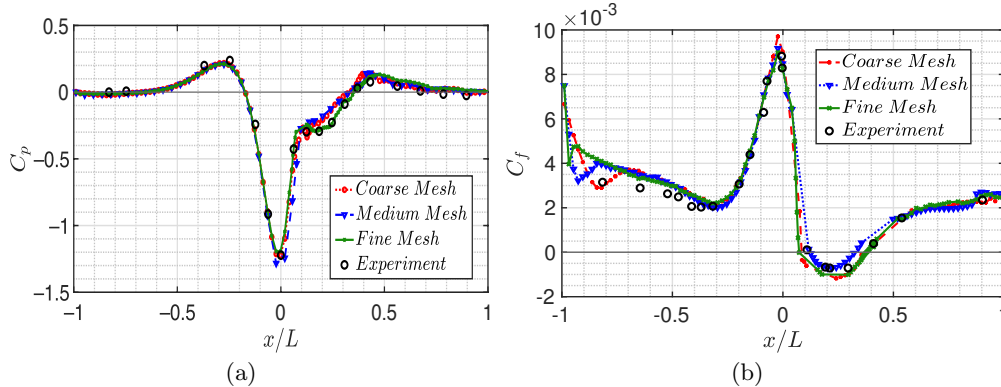


FIGURE 11. Streamwise distribution for the three-dimensional bump at  $Re_L = 3.4 \times 10^6$  of (a) the surface pressure coefficient and (b) the surface friction coefficient at midspan ( $z/L = 0$ ). The sensor-aided EQWM is applied, and three mesh resolutions are shown. The symbols for the pressure coefficient represent the experiments of Williams *et al.* (2020), and those for skin friction represent the experiments of Gray *et al.* (2021).

on the NASA transonic Common Research Model aircraft using the modeling approaches discussed in this brief compared to the standard DSM and EQWM approaches.

## 6. Conclusions

In this brief, we have developed and validated a predictive sensor to aid the equilibrium wall model in predicting the wall shear stress in the vicinity of and within the separation bubble. This sensor is agnostic to the choice of a subgrid-scale model and hence can be implemented and tested for a variety of flows of interest. The proposed sensor takes the information of the velocity and the pressure gradient from the matching location between the outer LES and EQWM to determine the extent of local non-equilibrium in the flow.

The performance of this sensor is tested in the flow over the Boeing speed bump at two Reynolds numbers,  $Re_L = 2 \times 10^6$  and  $3.4 \times 10^6$ . For both, comparisons against the previous work of Agrawal *et al.* (2022) suggest a clear improvement in the prediction of the quantities of interest such as the pressure and skin-friction coefficients across all considered grids. Monotonic convergence of the results is observed on grid refinement similar to that of Agrawal *et al.* (2022).

## Acknowledgments

The authors acknowledge support from NASA’s Transformational Tools and Technologies project grant, #80NSSC20M0201, and from Boeing Research & Technology. Computing resources were awarded through the Oak Ridge Leadership Computing Facility.

## Appendix. Limiting behavior of the dynamic sensor for equilibrium flows

In this appendix we investigate the limiting behavior of the dynamic sensor for turbulent channel flow, and a zero pressure gradient boundary layer.

Consider a turbulent channel flow ( $Re_\tau \gg 1$ ) with the coordinate axis aligned such

that the mean driving pressure gradient is active in  $x$  direction. From the definitions of  $u_p$  and  $u_\tau$ , the ratio of the two characteristic velocity scales can be written as

$$\frac{|\overline{u_\tau}|}{|\overline{u_p}|} \sim \frac{\sqrt{|\tau_w|/\rho}}{|(\frac{\mu}{\rho^2} \frac{\partial P}{\partial x})|^{1/3}}. \quad (1)$$

Furthermore, for a channel of half-height  $\delta$ , one can show that

$$|\tau_w| = \left| \frac{\partial P}{\partial x} \right| \delta. \quad (2)$$

Replacing Eq. (A 2) in Eq. (A 1) and expressing the quantities in inner units lead to the observation

$$\frac{|\overline{u_\tau}|}{|\overline{u_p}|} \sim (Re_\tau)^{1/3} = \left( \frac{u_\tau \delta}{\nu} \right)^{1/3}. \quad (3)$$

Thus, for a turbulent channel flow (wherein  $Re_\tau \gg 1$  is always satisfied) under equilibrium conditions, the proposed wall model will behave similarly to the EQWM. Numerous previous studies (Lozano-Durán & Bae 2019; Yang *et al.* 2017) have verified the ability of EQWM in predicting nearly accurate mean velocity profiles and Reynolds shear stresses in turbulent channel flows.

In a mean zero pressure gradient boundary layer, it is trivially true that in the mean  $u_\tau > u_p$ , and hence the wall model will behave similarly as the equilibrium wall model.

#### REFERENCES

- ADAMS, E. & JOHNSTON, J. 1988 Flow structure in the near-wall zone of a turbulent separated flow. *AIAA Journal*. **26**, 932–939.
- AGRAWAL, R., WHITMORE, M. P., GRIFFIN, K. P., BOSE, S. T. & MOIN, P. 2022 Non-Boussinesq subgrid-scale model with dynamic tensorial coefficients. *Phys. Rev. Fluids* **7**, 074602.
- AGRAWAL, R., WHITMORE, M. P., GRIFFIN, K. P. & MOIN, P. 2021 Dynamic modeling of non-Boussinesq subgrid-scale models for large-eddy simulations. *Annual Research Briefs*, Center for Turbulence Research, Stanford University, pp. 31–43.
- BAE, H. J., LOZANO-DURÁN, A., BOSE, S. T. & MOIN, P. 2019 Dynamic slip wall model for large-eddy simulation. *J. Fluid Mech.* **859**, 400–432.
- BALAKUMAR, P., PARK, G. I. & PIERCE, B. 2014 DNS, LES, and wall-modeled LES of separating flow over periodic hills. *Proceedings of the Summer Program*, Center for Turbulence Research, Stanford University, pp. 407–415.
- BOSE, S. T. & MOIN, P. 2014 A dynamic slip boundary condition for wall-modeled large-eddy simulation. *Phy. Fluids* **26**, 015104.
- BOSE, S. T. & PARK, G. I. 2018 Wall-modeled large-eddy simulation for complex turbulent flows. *Annu. Rev. Fluid Mech.* **50**, 535–561.
- BRÈS, G. A., BOSE, S. T., EMORY, M., HAM, F. E., SCHMIDT, O. T., RIGAS, G. & COLONIUS, T. 2018 Large-eddy simulations of co-annular turbulent jet using a Voronoi-based mesh generation framework.
- CABOT, W. & MOIN, P. 2000 Approximate wall boundary conditions in the large-eddy simulation of high Reynolds number flow. *Flow Turb. and Combust.* **63**, 269–291.
- CHOI, H. & MOIN, P. 2012 Grid-point requirements for large eddy simulation: Chapman’s estimates revisited. *Phy. Fluids* **24**, 011702.

- FU, L., KARP, M., BOSE, S. T., MOIN, P. & URZAY, J. 2021 Shock-induced heating and transition to turbulence in a hypersonic boundary layer. *J. Fluid Mech.* **909**, **A8**.
- GERMANO, M., PIOMELLI, U., MOIN, P. & CABOT, W. H. 1991 A dynamic subgrid-scale eddy viscosity model. *Phy. Fluids A-Fluid* **3**, 1760–1765.
- GHOSAL, S., LUND, T. S., MOIN, P. & AKSELVOLL, K. 1995 A dynamic localization model for large-eddy simulation of turbulent flows. *J. Fluid Mech.* **286**, 229–255.
- GOC, K., AGRAWAL, R., BOSE, S.T. & MOIN, P. 2022 Studies in Large Eddy Simulations of the Transonic NASA Common Research Model. *Annual Research Briefs*, Center for Turbulence Research, Stanford University. In press.
- GOC, K. A., LEHMKUHL, O., PARK, G. I., BOSE, S. T. & MOIN, P. 2021 Large eddy simulation of aircraft at affordable cost: a milestone in computational fluid dynamics. *Flow* **1**, E14.
- GRAY, P. D., GLUZMAN, I., THOMAS, F., CORKE, T., LAKEBRINK, M. & MEJIA, K. 2021 A new validation experiment for smooth-body separation. AIAA Paper 2021-2810.
- GRAY, P. D., GLUZMAN, I., THOMAS, F. O. & CORKE, T. C. 2022 Experimental characterization of smooth body flow separation over wall-mounted Gaussian bump. AIAA Paper 2022-1209.
- IYER, P. S. & MALIK, M. R. 2021 Wall-modeled LES of flow over a Gaussian bump. AIAA Paper 2022-1438.
- KAWAI, S. & LARSSON, J. 2012 Wall-modeling in large eddy simulation: length scales, grid resolution, and accuracy. *Phy. Fluids* **24**, 015105.
- LOZANO-DURÁN, A. & BAE, H. J. 2019 Error scaling of large-eddy simulation in the outer region of wall-bounded turbulence. *J. Comp. Phy.* **392**, 532–555.
- LOZANO-DURÁN, A., BOSE, S. T. & MOIN, P. 2020 Performance of wall-modeled LES for external aerodynamics in the NASA Junction Flow. *Annual Research Briefs*, Center for Turbulence Research, Stanford University, pp. 33–48.
- LOZANO-DURÁN, A., GIOMETTO, M. G., PARK, G. I. & MOIN, P. 2020 Non-equilibrium three-dimensional boundary layers at moderate Reynolds numbers. *J. Fluid Mech.* **883**, **A20**.
- LOZANO-DURÁN, A. & JIMÉNEZ, J. 2014 Effect of the computational domain on direct simulations of turbulent channels up to  $Re_\tau = 4200$ . *Phy. Fluids* **26**, 011702.
- MENEVEAU, C., LUND, T. S. & CABOT, W. H. 1996 A Lagrangian dynamic subgrid-scale model of turbulence. *J. Fluid Mech.* **319**, 353–385.
- MOIN, P., SQUIRES, K., CABOT, W. & LEE, S. 1991 A dynamic subgrid-scale model for compressible turbulence and scalar transport. *Phy. Fluids A-Fluid*, 2746–2757.
- NICOUD, F., TODA, H. B., CABRIT, O., BOSE, S. & LEE, J. 2011 Using singular values to build a subgrid-scale model for large eddy simulations. *Phy. Fluids* **23**, 085106.
- ROZEMA, W., BAE, H. J., MOIN, P. & VERSTAPPEN, R. 2015 Minimum-dissipation models for large-eddy simulation. *Phy. Fluids* **27**, 085107.
- SIMPSON, R. L. 1983 A model for the backflow mean velocity profile. *AIAA J.* **21**, 142–143.
- SMAGORINSKY, J. 1963 General circulation experiments with the primitive equations: I. the basic experiment. *Mon. Weather Rev.* **91**, 99–164.
- UZUN, A. & MALIK, M. R. 2022 High-fidelity simulation of turbulent flow past Gaussian bump. *AIAA J.* **60**, 2130–2149.

- VREMAN, A. W. 2004 An eddy-viscosity subgrid-scale model for turbulent shear flow: algebraic theory and applications. *Phy. Fluids* **16**, 3670–3681.
- VREMAN, B., GEURTS, B. & KUERTEN, H. 1994 On the formulation of the dynamic mixed subgrid-scale model. *Phy. Fluids* **6**, 4057–4059.
- WHITMORE, M. P., GRIFFIN, K. P., BOSE, S. T. & MOIN, P. 2021 Large-eddy simulation of a Gaussian bump with slip-wall boundary conditions. *Annual Research Briefs*, Center for Turbulence Research, Stanford University, pp. 45–58.
- WILLIAMS, O., SAMUELL, M., SARWAS, E. S., ROBBINS, M. & FERRANTE, A. 2020 Experimental study of a CFD validation test case for turbulent separated flows.
- YANG, X., SADIQUE, J., MITTAL, R. & MENEVEAU, C. 2015 Integral wall model for large eddy simulations of wall-bounded turbulent flows. *Phy. Fluids* **27**, 025112.
- YANG, X. I. A., PARK, G. I. & MOIN, P. 2017 Log-layer mismatch and modeling of the fluctuating wall stress in wall-modeled large-eddy simulations. *Phy. Rev. Fluids* **2**, 104601.